Optical conductivity of the Weyl semimetal NbP

David Neubauer,[1] Alexander Yaresko,[2] Weiwu Li,[1] Anja Löhle,[1] Ralph Hübner,[1,3] Micha B. Schilling,[1] Chandra Shekhar,[4] Claudia Felser,[4] Martin Dressel,[1] and Artem V. Pronin[1]

[1]*1. Physikalisches Institut, Universität Stuttgart, 70569 Stuttgart, Germany*

[2]*Max-Planck-Institut für Festkörperforschung, Heisenbergstr. 1, 70569 Stuttgart, Germany*

[3]*Biomedical Chemistry, Department of Clinical Radiology and Nuclear Medicine, Medical Faculty Mannheim of Heidelberg University, 68167 Mannheim, Germany*

[4]*Max-Planck-Institut für Chemische Physik fester Stoffe, 01187 Dresden, Germany*

(Received 26 March 2018; published 7 November 2018)

The optical properties of (001)-oriented NbP single crystals have been studied in a wide spectral range from 6 meV to 3 eV from room temperature down to 10 K. The itinerant carriers lead to a Drude-like contribution to the optical response; we can further identify two pronounced phonon modes and interband transitions starting already at rather low frequencies. By comparing our experimental findings to the calculated interband optical conductivity, we can assign the features observed in the measured conductivity to certain interband transitions. In particular, we find that transitions between the electronic bands spilt by spin-orbit coupling dominate the interband conductivity of NbP below 100 meV. At low temperatures, the momentum-relaxing scattering rate of itinerant carriers in one of the conduction channels is very small, leading to mesoscopic (hundreds of nanometers) characteristic length scales for momentum relaxation.

DOI: 10.1103/PhysRevB.98.195203

I. INTRODUCTION

NbP is a nonmagnetic noncentrosymmetric Weyl semimetal (WSM) with extremely large magnetoresistance and ultrahigh carrier mobility [1,2]. These extraordinary transport properties are believed to be caused by quasiparticles in linearly dispersing Weyl bands [3,4]. According to band-structure calculations, NbP possesses 24 Weyl nodes, i.e., 12 pairs of the nodes with opposite chiralities [3–7]. The nodes are "leftovers" of nodal rings, which are gapped by spin-orbit coupling (SOC) everywhere in the Brillouin zone (BZ), except for these special points [3,5,6,8]. The nodes can be divided in two groups, commonly dubbed as W1 ($N_{W1} = 8$) and W2 ($N_{W2} = 16$); here $N_{W1,2}$ is the number of nodes of each type. Most recent band-structure calculations agree well on the energy position of the W1 nodes: 56–57 meV below the Fermi level E_F [9–11]; the position of the W2 nodes is specified less accurately, ranging from 5 [9,10] to 26 meV [11] above E_F. Furthermore, the W2 cones could be strongly tilted along a low-symmetric direction in the BZ [10], thus realizing a type-II WSM state [12,13].

Similar to all WSMs, physical properties of NbP are mostly determined by the low-energy electron dynamics [14,15]. Infrared optical methods enable direct access to this dynamics. For example, the interband optical response of a single isotropic three-dimensional Weyl band, being expressed in terms of the real part of the complex conductivity, should follow a linear frequency dependence with the prefactor given by the band Fermi velocity v_F [16–18]:

$$\sigma(\omega) = \frac{e^2}{12h}\frac{\omega}{v_F}. \quad (1)$$

Here, electron-hole symmetry is assumed, and the complex conductivity is $\hat{\sigma}(\omega) = \sigma(\omega) - i\omega(\varepsilon(\omega) - 1)/4\pi$, with $\varepsilon(\omega)$ the real part of the dielectric function. For N_W identical Weyl bands, the right side of Eq. (1) should be multiplied by N_W. Such a linear behavior of the optical conductivity ($\sigma \propto \omega$) has indeed been observed in a number of well-established and proposed three-dimensional Weyl/Dirac-semimetal systems [19–26].

For this paper, we have measured and analyzed both interband and itinerant-carrier conductivity of NbP. We show that the low-energy interband conductivity of NbP is dominated by transitions between the bands with parallel dispersions that are split by SOC. These excitations, as well as the Drude response of the itinerant carriers, completely mask the linear-in-frequency $\sigma(\omega)$ due to the three-dimensional chiral Weyl bands. At somewhat higher frequencies (1400–2000 cm^{-1}, 175–250 meV), $\sigma(\omega)$ becomes roughly linear. Our calculations demonstrate that this linearity stems from the fact that all electronic bands, which are involved in the transitions with relevant energies, are roughly linear. In addition, we find that at low temperatures the itinerant carriers in one of the conduction channels possess a fairly long momentum-relaxing scattering time and mesoscopic characteristic length scales of momentum relaxation.

II. SAMPLE PREPARATION, EXPERIMENTAL AND COMPUTATIONAL DETAILS

Single crystals of NbP were synthesized according to the description reported in Refs. [1,27]: a polycrystalline NbP powder was synthesized in a direct reaction of pure niobium and red phosphorus; the single NbP crystals were grown from the powder via vapor-transport reaction with iodine.

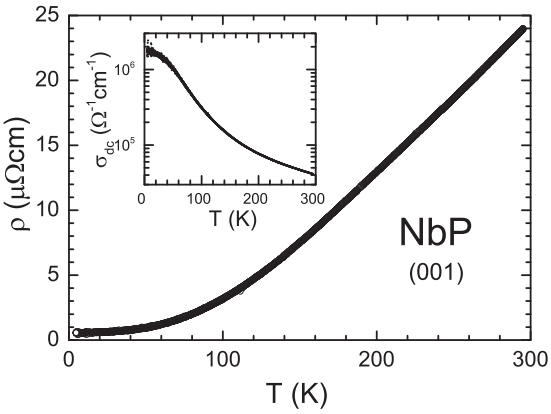

FIG. 1. Temperature-dependent (001)-plane dc resistivity of the NbP sample used in the optical measurements. The inset shows dc conductivity.

The electrical resistivity, $\rho_{dc}(T)$, was measured as a function of temperature within the (001)-plane in four-contact geometry. The experiments were performed on a small piece, cut from the specimen used for the optical investigations. The results of the dc measurements are plotted in Fig. 1. A clear metallic behavior with linear-in-temperature resistivity is observed down to approximately 100 K. Below, $\rho_{dc}(T)$ levels off and approaches the residual resistivity $\rho_0 = 0.55\ \mu\Omega$cm; the resistivity ratio is $\rho(300\,\mathrm{K})/\rho_0 = 40$. These values are well comparable with the ones reported in literature [1,2,28]. Note, NbP exhibits an extremely high mobility independent on the residual resistivity ratio [2].

The normal-incidence optical reflectivity $R(\nu, T)$ was measured on the (001)-surfaces of a large (2 mm × 2 mm in lateral dimensions) single crystal from room temperature down to $T = 10$ K covering a wide frequency range from $\nu = \omega/(2\pi c) = 50$ to $12\,000\,\mathrm{cm}^{-1}$. The temperature-dependent experiments were supplemented by room-temperature reflectivity measurements up to $25\,000\,\mathrm{cm}^{-1}$. In the far-infrared spectral range below $700\,\mathrm{cm}^{-1}$, a Bruker IFS 113v Fourier-transform spectrometer was employed with *in situ* gold coating of the sample surface for reference measurements. At higher frequencies, we used a Bruker Hyperion infrared microscope attached to a Bruker Vertex 80v spectrometer. Here, freshly evaporated gold mirrors (below $12\,000\,\mathrm{cm}^{-1}$) and protected silver (above $12\,000\,\mathrm{cm}^{-1}$) served as reference.

For the Kramers-Kronig analysis [29,30], we involved the x-ray atomic scattering functions for high-frequency extrapolations [31]. From recent optical investigations of materials with highly mobile carriers, it is known [32,33] that the commonly applied Hagen-Rubens extrapolation to zero frequency is not adequate: the very narrow zero-frequency component present in the spectra corresponds to a scattering rate comparable to (or even below) our lowest measurement frequency, $\nu_{\mathrm{min}} \approx 50\,\mathrm{cm}^{-1}$ (see also discussion in the next section). Thus, we first fitted the spectra with a set of Lorentzians (similar fitting procedures can be utilized as a substitute of the Kramers-Kronig analysis [34,35]) and then we used the results of these fits between $\nu = 0$ and ν_{min} as zero-frequency extrapolations for subsequent Kramers-Kronig transformations. We note that our optical measurements probe the bulk material properties, as the penetration depth exceeds 20 nm for any measurement frequency.

We performed band-structure calculations within the local density approximation based on the crystal structure of NbP determined by experiments [36]; we employed the linear muffin-tin orbital method [37] as implemented in the relativistic PY LMTO computer code. Some details of the implementation can be found in Ref. [38]. The Perdew-Wang parametrization [39] was used for the exchange-correlation potential. SOC was added to the LMTO Hamiltonian in the variational step. BZ integrations were done using the improved tetrahedron method [40]. Dipole matrix elements for interband optical transitions were calculated on a 96 × 96 × 96 k-mesh using LMTO wave functions. As was shown in Ref. [41], it is necessary to use sufficiently dense meshes to resolve transitions between the SOC-split bands. The real part of the optical conductivity was calculated by the tetrahedron method.

III. RESULTS AND ANALYSIS

Figure 2 displays the overall reflectivity $R(\nu)$, the real part of the conductivity $\sigma(\nu)$, and the dielectric constant $\varepsilon(\nu)$ of NbP for different temperatures. For frequencies higher than $5000\,\mathrm{cm}^{-1}$, the optical properties are basically independent on temperature. In the spectra we can identify the signatures of (i) phonons, (ii) itinerant-carrier (intraband) absorption, and (iii) interband transitions. Below we discus all these spectral features.

A. Phonons

In the far-infrared range, two sharp phonon peaks can be seen in Fig. 2 at 336 and $370\,\mathrm{cm}^{-1}$. Due to their symmetric shape, they can be nicely fitted with Lorentzians, as demonstrated in Fig. 2(e). This is in contrast to the highly asymmetric phonon resonances observed in the optical measurements of TaAs, where, unlike in our measurements on NbP, the probing radiation propagated along the low-symmetry [107] and [112] crystallographic directions [42].

In NbP, four infrared-active phonons are expected [43]; however, there is no full consensus on the calculated frequencies [43,44]. The phonon positions observed in our spectra agree very well with the calculations from Ref. [44] as well as with the Raman data presented there (in noncentrosymmetric structures, same phonon modes can be both, infrared and Raman, active). Thus, following Ref. [44], we assign the observed features at 336 and $370\,\mathrm{cm}^{-1}$ to those lattice vibrations that mainly involve the light P atoms. The other two infrared-active phonon modes are apparently too weak to be resolved on the electronic background.

B. Itinerant charge carriers

At the lowest frequencies, NbP exhibits an optical response typical for metals, i.e., the itinerant carriers dominate: the reflectivity approaches unity, $\varepsilon(\omega)$ is negative and diverges as $\omega \to 0$, $\sigma(\omega)$ exhibits a narrow zero-frequency peak, as seen in Figs. 2(a)–2(c). Figure 2(d) clearly shows a shoulder on this peak that can be fitted by a Lorentzian; it will be discussed in the next section.

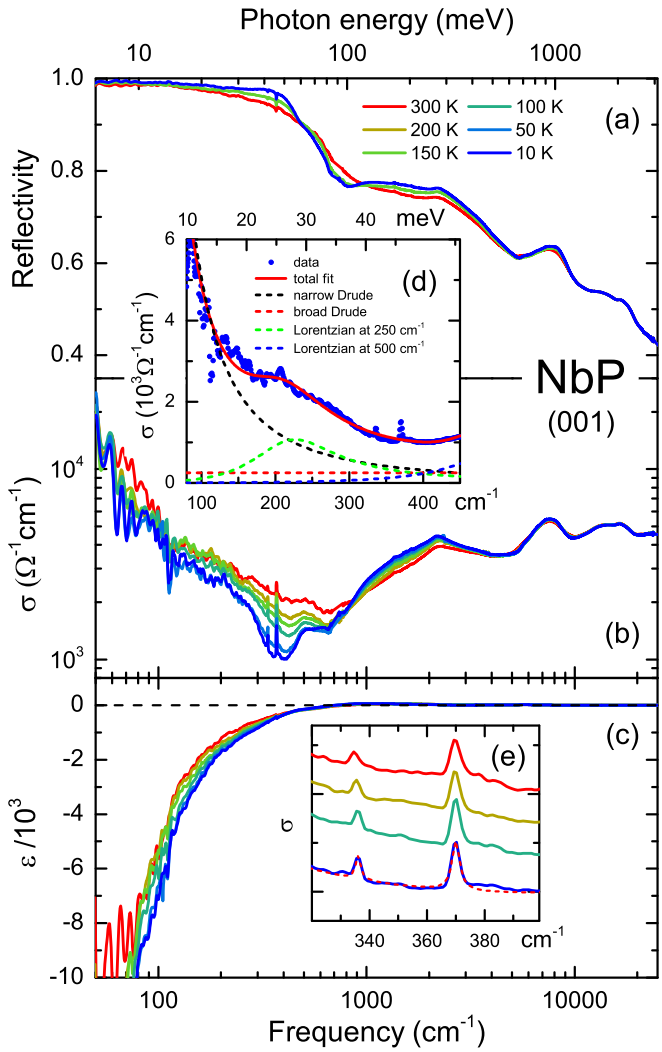

FIG. 2. (a) Optical reflectivity, real parts of the (b) optical conductivity and (c) dielectric permittivity of NbP at selected temperatures between $T = 10$ and 300 K; note the logarithmic frequency scale. The inset (d) shows a simple fit of the low-energy $\sigma(\nu)$ at $T = 10$ K by the sum of two Drude terms (narrow and broad) and two Lorentzians centered at 250 and 500 cm^{-1}, which mimic interband transitions. The inset (e) displays the phonon modes in $\sigma(\nu)$ on an enlarged frequency scale. The dashed red line corresponds to a fit of the features at $T = 10$ K by two narrow Lorentzians centered at 336 and 370 cm^{-1}, respectively.

The increase in $\sigma(\omega)$ at $\omega \to 0$ is large [note logarithmic vertical scale in Fig. 2(b)], but still the values of $\sigma(\omega)$ at our lowest frequency are below the dc values, cf. the inset of Fig. 1. This means that the optical conductivity experiences a drastic increase at the frequencies below our measurement window. Such behavior of $\sigma(\omega)$ is expected in materials with high carrier mobility and has been reported, e.g., in TaAs [24], YbPtBi [32], and $YbMnBi_2$ [41]. We can hence conclude that the ultrahigh mobility of NbP [1,2] provides a narrow Drude-like mode in $\sigma(\omega)$. This mode can indeed be fitted with a simple Drude model using the measured dc-conductivity values as zero-frequency extrapolations.

To make the analysis more accurate, we used a Drude-Lorentz approach [30] to fit $\hat{\sigma}(\omega)$ at low energies. We found that two Drude terms and two Lorentzians can accurately describe the spectra at frequencies $\leqslant 500$ cm^{-1}, Fig. 2(d) [at higher frequencies, Lorentzians are not an adequate description of the interband transitions, as will be discussed further].

In NbP, four bands cross the Fermi level, see Refs. [6,8] and also our calculations below. Nevertheless, two Drude terms are sufficient to account for the contribution of itinerant carriers into optical conductivity. Utilizing more Drude terms will only lead to ambiguities in determination of the fit parameters. Such a minimalist approach is common in optical-conductivity studies and has widely been used for different multiband systems [11,41,45–47]. For NbP, the two-Drude approach is justified by the effectively two-channel conduction in this compound [1]. Highly mobile carriers in crossing linear bands manifest themselves as a narrow Drude mode (small scattering rates), while low-mobile carriers in parabolic bands contribute as a broad Drude term (larger scattering rates). Such two-channel optical conductivity seems to be natural for (topological) semimetals and has been recently reported, e.g., in YbPtBi [32].

From the fits, we can determine the (momentum-relaxing) scattering rate γ_{mr} of the narrow Drude term, i.e., of the highly mobile carriers. The broad Drude term vastly overlaps with the interband transitions, thus determination of the scattering rate of low-mobile carriers is impossible. We have found γ_{mr} to be as low as 4.5 cm^{-1} at $T = 10$ K. The corresponding scattering time is $\tau_{\mathrm{mr}} = 1/(2\pi c \gamma_{\mathrm{mr}}) = 1.2$ ps and the momentum-relaxation length, $\ell_{\mathrm{mr}} = v_{\mathrm{F}}\tau_{\mathrm{mr}}$, becomes as long as 0.2 to 0.6 μm. Here we utilized the lower, 1.5×10^5 m/s, and, respectively, the upper, 4.8×10^5 m/s, boundaries for the (001)-plane Fermi velocity v_{F} obtained from experiment [1,2] and theory [6,8]. At elevated temperatures, γ_{mr} rises, reaching 35 cm^{-1} at $T = 300$ K. This corresponds to ℓ_{mr} of 20 to 70 nm. Let us note that because the scattering rates of the narrow Drude term are below our measurement frequency window, the vales obtained in this paragraph can only be considered as order-of-magnitude estimates.

C. Interband transitions: Optical experiments and calculations based on the electronic band structure

Calculations of the interband optical conductivity based on calculated electronic band structure are very useful, but seem to be rather challenging in (topological) semimetals. A survey of the available literature reveals only a qualitative match between the calculated optical conductivity and experimental results [11,25,41,48]. In the most interesting low-energy part of the spectrum (less than a few hundred meV), a reasonable agreement is particularly hard to achieve [25,41]. In the case of NbP, we have reached a fairly good qualitative match between our calculations of the optical conductivity and experimental spectra even at low energies; this allows us to identify the origin of various spectral features observed in $\sigma(\omega)$.

In Fig. 3, we compare the experimental low-temperature optical conductivity to the interband (001)-plane conductivity calculated with and without SOC. Note that the itinerant-carriers contributions have not been subtracted from the experimental conductivity. The calculated spectra qualitatively agree with the experiment: the inset in Fig. 3 illustrates

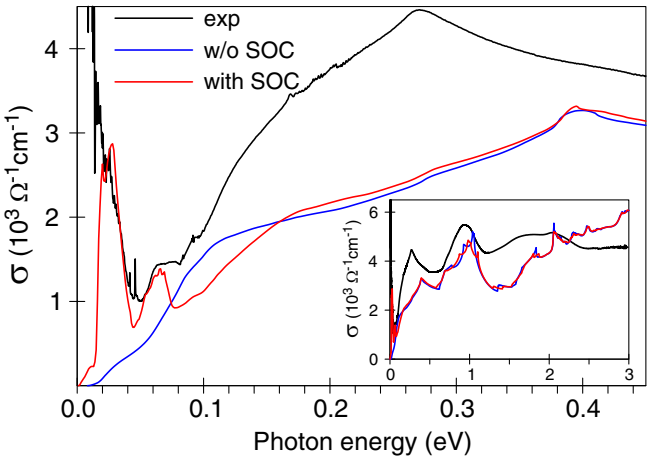

FIG. 3. Interband optical conductivity of NbP calculated with (red line) and without (blue line) SOC and the total experimental NbP conductivity at 10 K (black line). Intraband (Drude) contributions to the conductivity are not included in the computations. Inset shows same sets of data on a broader photon energy scale (0–3 eV). All spectra are for the (001)-plane response.

that the peaks and deeps in the calculated $\sigma(\omega)$ reasonably coincide with those in the experimental data. The calculated spectra contain more fine structures than the experimental $\sigma(\omega)$, as no broadening was applied to the computed spectra in order to simulate finite life-time effects.

Above an energy of 0.2 eV, the effect of SOC on the theoretical $\sigma(\omega)$ is negligible; but for smaller energies the spectra computed with and without taking SOC into account differ significantly. The interband contribution to the conductivity calculated without SOC increases smoothly when raising the photon energy to 0.1 eV. When SOC is included, however, two sharp peaks appear around 30 and 65 meV (corresponding to ∼250 and 500 cm^{-1}). The latter matches very well the shoulder we observed on the narrow Drude term, as shown in Fig. 2(d). The former feature can be directly associated with the bump observed at all temperatures at around 500 cm^{-1} in the measured spectra plotted in Fig. 2(b). The fact that these two peaks appear only in those calculations including SOC indicates that they must be related to the transitions between the SOC-split bands.

Our conclusion gets support when decomposing the calculated $\sigma(\omega)$ into contributions coming from transitions between different pairs of bands crossing E_F. When SOC is neglected, two doubly degenerate bands with predominant Nb d character cross on a $k_{x/y} = 0$ mirror plane and form one electron and one hole Fermi surface with crescent-shaped cross sections by this plane [6]. This degeneracy is lifted

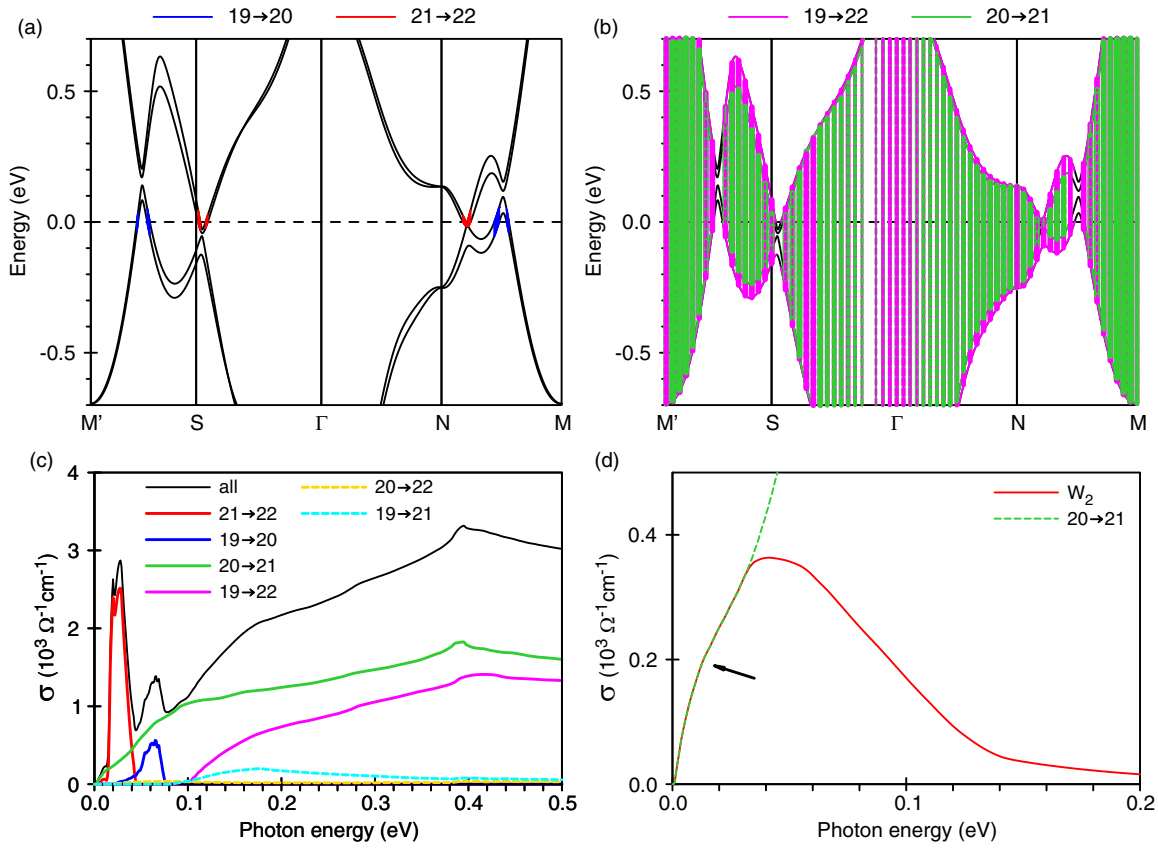

FIG. 4. (a), (b) Band structure of NbP along selected lines in the BZ with allowed transitions shown as colored vertical lines. The thickness of the lines is proportional to the transition probability. (c) Calculated contributions to the interband conductivity from transitions between different pairs of bands crossing E_F, as indicated, and the total calculated interband conductivity of NbP. (d) Contribution to $\sigma_{20\to21}(\omega)$ from the transitions within the small volumes in **k**-space, enclosing the W2 Weyl points (red solid line, see text for details), in comparison with the total $\sigma_{20\to21}(\omega)$ (dashed green line). The arrow indicates a kink, which corresponds to the point, where the chiral Weyl bands merge.

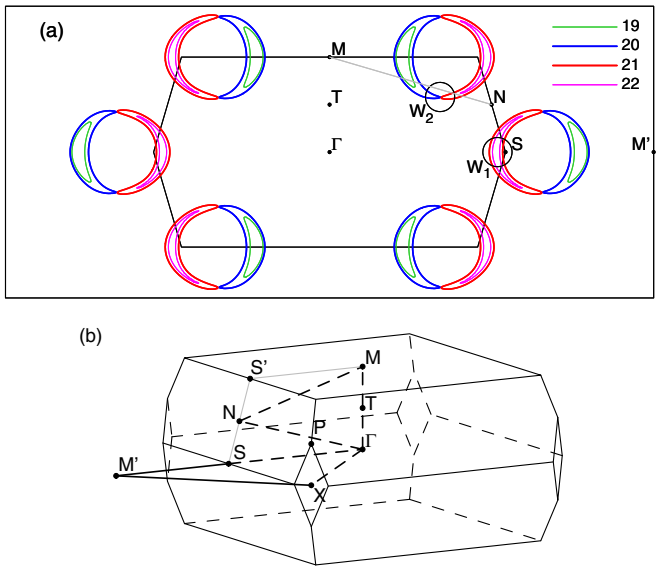

FIG. 5. (a) Fermi surface cross sections by $k_y = 0$ plane. Small black circles illustrate integration volumes around Weyl points. (b) BZ of NbP. Weyl points from the W1 set are situated near the S point, while the points from the W2 set are close to the N–M line.

when SOC is accounted for; thus, four nondegenerate bands, numbered 19 to 22, now cross E_F as shown in Figs. 4 and 5 (at every given **k** point, the bands are numbered with increasing energy). The band structure of NbP, calculated along selected lines in the BZ [cf. Fig. 5(b)], and the allowed transitions between different bands are shown in Figs. 4(a) and 4(b). Here, the thickness of the vertical lines connecting occupied initial and unoccupied final states is proportional to the probability of the interband transition at a given **k** point. In Fig. 4(c), we plot the various contributions to the total interband conductivity from all individual interband transitions: $19 \to 20$, $19 \to 21$, $19 \to 22$, $20 \to 21$, $20 \to 22$, and $21 \to 22$.

The bands can be characterized by their spin polarization $\langle s \rangle$, which is well defined, i.e., $\langle s \rangle \simeq \pm 1/2$, only for **k**-vectors faraway from the band-crossing points. Closer to the band crossings, SOC effects are strong and spin polarization is much less perfect. Thus, transitions between any pair of bands are allowed here. The transitions $19 \to 21$ and $20 \to 22$ (the bands in each pair here possess opposite spin characters away from the nodes) still provide very small contributions to the optical conductivity [dashed cyan and yellow lines in Fig. 4(c)] because the allowed low-frequency transitions near the nodes are Pauli-blocked and the transition probability diminishes with increasing frequency.

For other pairs of bands with predominantly opposite spin characters ($19 \to 20$ and $21 \to 22$), the situation is different. The pronounced narrow peak at 30 meV is formed by transitions between bands 21 and 22 [red line in Fig. 4(c)], while the 65 meV mode is due to the $19 \to 20$ transitions [blue line]; i.e., both features stem from transitions between SOC-split bands. These transitions are only allowed in a small volume of the **k**-space, where one of the two SOC-split bands is occupied, while the other one is empty [see the red and blue lines in Fig. 4(a)], i.e., between the nested crescents in Fig. 5(a). Within this volume, the SOC-split bands are almost parallel to each other. This ensures the appearance of strong and narrow peaks in the joint density of states for the corresponding interband transitions. The peak positions are determined by the average band splitting, which, in turn, is of the order of the SOC strength of the Nb d states, $\xi_d \approx 85$ meV. Finally, since the dipole matrix elements for these transitions are rather large, the two peaks dominate the low-energy interband conductivity.

Besides these two peaks, there are also significant contributions to the optical conductivity with a smooth ω dependence. These contributions originate in transitions between the touching bands 20 and 21 [green lines in Figs. 4(b) and 4(c)] and between bands 19 and 22, which are separated by a finite gap everywhere in the BZ [magenta lines]. Accordingly, $\sigma_{20\to21}(\omega)$ starts at zero energy, while $\sigma_{19\to22}(\omega)$ at 0.1 eV. Both conductivity contributions, $\sigma_{20\to21}$ and $\sigma_{19\to22}$, increase, when the photon energy rises from 0 to 0.4 eV. Both contributions, $\sigma_{19\to22}$ and $\sigma_{19\to22}$, as well as the total calculated $\sigma(\omega)$ exhibit sharp kinks (Van Hove singularities [49]) at 0.4 eV, which are related to the transitions between flat parallel bands near the N point, see Fig. 4(b). The experimental $\sigma(\omega)$ demonstrates such a kink at somewhat lower energy, 0.27 eV (Fig. 3); still, we find this match reasonable.

In the vicinity of a Weyl point, the optical conductivity is expected to be proportional to frequency, Eq. (1). The two sets of Weyl points in NbP, W1 and W2, are formed by the touching points of bands 20 and 21. In agreement with previous results [6,9–11], our LMTO calculations yield the W1 points approximately 50 meV below E_F. Consequently, their contribution to the conductivity cannot start at zero frequency [18]. On the other hand, the energy of the W2 points in the present calculations is very close to E_F and, thus, transitions near W2 may provide a linearly vanishing $\sigma(\omega)$ as $\omega \to 0$. To verify this behavior, we calculate the contribution to $\sigma_{20\to21}(\omega)$ from a **k** volume with a radius of $\sim 0.05\frac{2\pi}{a}$ (a is the in-plane lattice constant) around the averaged position of a pair of W2 points. The contribution indeed shows a linear ω dependence as $\omega \to 0$, see Fig. 4(d). The smooth kink at $\sim$15 meV, marked with an arrow, corresponds to the merging point of the chiral Weyl bands [49,50]. We should note that in experiments, this linear interband optical conductivity at low ω is completely masked by the itinerant carriers and by the strong peaks due to the transitions between the SOC-split bands, as discussed above.

Although no linear-in-frequency $\sigma(\omega)$ due to the transitions within the chiral Weyl bands can be seen in NbP at low frequencies, both, experimental and computed, $\sigma(\omega)$ demonstrate a sort of linear increase with ω at higher frequencies: 180 to 250 meV for the experimental and up to 360 meV for the calculated optical conductivity, see Fig. 3. As apparent from our calculations, the linearity just reflects the fact that all the electronic bands, involved in the transitions with corresponding energies, are roughly linear (but not parallel to each other), see Fig. 4(b).

Based on the comparison between the calculated and the experimental conductivity, we can assign the observed spectral features to different absorption mechanisms. Figure 6 schematically summarizes these assignments.

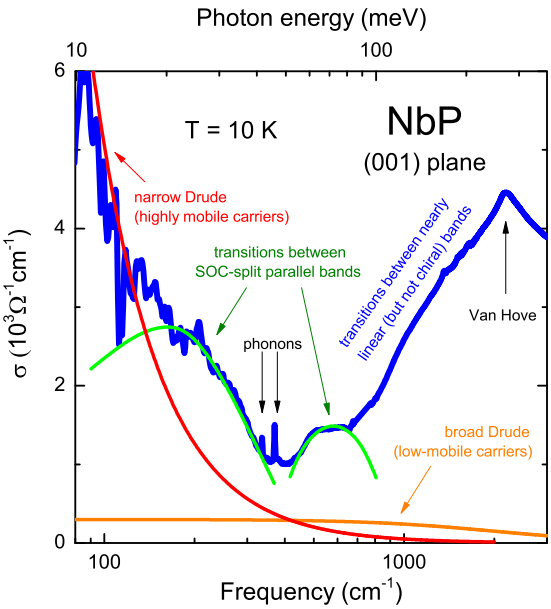

FIG. 6. Low-frequency portion of the real part of NbP optical conductivity at 10 K and assignment of the observed features to different absorption mechanisms, as discussed in the course of this paper. Note that the contributions of these mechanisms are shown schematically; for example, the scattering rate of the broad Drude mode is ill defined.

Before we conclude, we would like to emphasize the importance of the transitions between the SOC-split bands. So far, the strong influence of these transitions on the low-energy conductivity of WSMs has not been fully appreciated. Using a modified Dirac Hamiltonian [14], Tabert and Carbotte [50] calculated the optical conductivity for a four-band model, relevant for many WSMs. In this model, the band structure consists of four isotropic nondegenerate three-dimensional bands, two of which cross and the other two are gapped. The band structure is mirror symmetric in energy with respect to the Weyl nodes and the Weyl cones are anisotropic in **k**-space at low energies. This model definitely grasps the main features of the band structure of many WSMs, including those from the TaAs family; but—apart from neglecting possible band anisotropy—it does not take into account the transitions between the SOC-split bands: these transitions are considered forbidden in the model, while in the real WSMs they might play an important role, as we have shown for NbP.

Finally, we would like to note that TaAs and TaP demonstrate sharp absorption peaks at frequencies, which compare well to those of the transitions between the SOC-split bands in NbP, cf. Fig. 3 from Ref. [25]. Previously, these features have been assigned to transitions between the merging (saddle) points of the Weyl bands, even though, e.g., in TaP this assignment is at odds with the absence of chiral carriers [51]. We suggest reconsidering this assignment.

IV. CONCLUSIONS

We measure and analyze the interband and itinerant-carrier optical conductivity of NbP. From the electronic band structure, we calculate the interband optical conductivity and decompose it into contributions from the transitions between different bands. By comparing these contributions to the spectral features in the experimental conductivity, we assign the observed features to certain interband transitions. We argue that the low-energy (below 100 meV) interband conductivity is dominated by transitions between almost parallel bands, split by SOC. Hence, these transitions manifest themselves as relatively sharp peaks centered at 30 and 65 meV. These peaks and the low-energy itinerant-carrier conductivity (Drude-like) conceal the linear-in-frequency contribution to $\sigma(\omega)$ from the transitions within the chiral Weyl bands. Our calculations demonstrate that the nearly linear in ω conductivity at around 200–300 meV is naturally explained by the fact that all electronic bands involved in the transitions with such frequencies possess approximately linear dispersion relations. We also identify two optical phonons and assign them to the vibrations, which mostly involve P atoms. Finally, we find that the itinerant carriers at least in one of the conduction channels possess very low momentum-relaxing scattering rates at low temperatures, leading to mesoscopic characteristic lengths (hundreds of nanometers) of momentum relaxation.

ACKNOWLEDGMENTS

We thank Gabriele Untereiner and Sabine Prill-Diemer for technical support, as well as Johannes Gooth, Dmitri Efremov, Uwe Pracht, and Hongbin Zhang for fruitful discussions. This project was funded by the Deutsche Forschungsgesellschaft via Grant No. DR228/51-1.

[1] C. Shekhar, A. K. Nayak, Y. Sun, M. Schmidt, M. Nicklas, I. Leermakers, U. Zeitler, Y. Skourski, J. Wosnitza, Z. Liu, Y. Chen, W. Schnelle, H. Borrmann, Y. Grin, C. Felser, and B. Yan, Nat. Phys. **11**, 645 (2015).

[2] Z. Wang, Y. Zheng, Z. Shen, Y. Lu, H. Fang, F. Sheng, Y. Zhou, X. Yang, Y. Li, C. Feng, and Z.-A. Xu, Phys. Rev. B **93**, 121112(R) (2016).

[3] S.-M. Huang, S.-Y. Xu, I. Belopolski, C.-C. Lee, G. Chang, B. K. Wang, N. Alidoust, G. Bian, M. Neupane, C. Zhang, S. Jia, A. Bansil, H. Lin, and M. Z. Hasan, Nat. Commun. **6**, 7373 (2014).

[4] D.-F. Xu, Y.-P. Du, Z. Wang, Y.-P. Li, X.-H. Niu, Q. Yao, P. Dudin, Z.-A. Xu, X.-G. Wan, and D.-L. Feng, Chin. Phys. Lett. **32**, 107101 (2015).

[5] H. Weng, C. Fang, Z. Fang, B. A. Bernevig, and X. Dai, Phys. Rev. X **5**, 011029 (2015).

[6] C.-C. Lee, S.-Y. Xu, S.-M. Huang, D. S. Sanchez, I. Belopolski, G. Chang, G. Bian, N. Alidoust, H. Zheng, M. Neupane, B. Wang, A. Bansil, M. Z. Hasan, and H. Lin, Phys. Rev. B **92**, 235104 (2015).

[7] Y. Sun, S.-C. Wu, and B. Yan, Phys. Rev. B **92**, 115428 (2015).

[8] K.-H. Ahn, K.-W. Lee, and W. E. Pickett, Phys. Rev. B **92**, 115149 (2015).

[9] J. Klotz, S.-C. Wu, C. Shekhar, Y. Sun, M. Schmidt, M. Nicklas, M. Baenitz, M. Uhlarz, J. Wosnitza, C. Felser, and B. Yan, Phys. Rev. B **93**, 121105(R) (2016).

[10] S.-C. Wu, Y. Sun, C. Felser, and B. Yan, Phys. Rev. B **96**, 165113 (2017).

[11] D. Grassano, O. Pulci, A. M. Conte, and F. Bechstedt, Sci. Rep. **8**, 3534 (2018).

[12] A. A. Soluyanov, D. Gresch, Z. Wang, Q. Wu, M. Troyer, X. Dai, and B. A. Bernevig, Nature **527**, 495 (2015)

[13] Y. Xu, F. Zhang, and C. Zhang, Phys. Rev. Lett. **115**, 265304 (2015).

[14] A. A. Burkov, M. D. Hook, and L. Balents, Phys. Rev. B **84**, 235126 (2011).

[15] T. O. Wehling, A. M. Black-Schaffer, and A. V. Balatsky, Adv. Phys. **63**, 1 (2014).

[16] P. Hosur, S. A. Parameswaran, and A. Vishwanath, Phys. Rev. Lett. **108**, 046602 (2012).

[17] Á. Bácsi and A. Virosztek, Phys. Rev. B **87**, 125425 (2013).

[18] P. E. C. Ashby and J. P. Carbotte, Phys. Rev. B **89**, 245121 (2014).

[19] T. Timusk, J. P. Carbotte, C. C. Homes, D. N. Basov, and S. G. Sharapov, Phys. Rev. B **87**, 235121 (2013).

[20] R. Y. Chen, S. J. Zhang, J. A. Schneeloch, C. Zhang, Q. Li, G. D. Gu, and N. L. Wang, Phys. Rev. B **92**, 075107 (2015).

[21] A. B. Sushkov, J. B. Hofmann, G. S. Jenkins, J. Ishikawa, S. Nakatsuji, S. Das Sarma, and H. D. Drew, Phys. Rev. B **92**, 241108(R) (2015).

[22] K. Ueda, J. Fujioka, and Y. Tokura, Phys. Rev. B **93**, 245120 (2016).

[23] D. Neubauer, J. P. Carbotte, A. A. Nateprov, A. Löhle, M. Dressel, and A. V. Pronin, Phys. Rev. B **93**, 121202(R) (2016).

[24] B. Xu, Y. M. Dai, L. X. Zhao, K. Wang, R. Yang, W. Zhang, J. Y. Liu, H. Xiao, G. F. Chen, A. J. Taylor, D. A. Yarotski, R. P. Prasankumar, and X. G. Qiu, Phys. Rev. B **93**, 121110(R) (2016).

[25] S. I. Kimura, H. Yokoyama, H. Watanabe, J. Sichelschmidt, V. Süß, M. Schmidt, and C. Felser, Phys. Rev. B **96**, 075119 (2017).

[26] F. Hütt, A. Yaresko, M. B. Schilling, C. Shekhar, C. Felser, M. Dressel, and A. V. Pronin, Phys. Rev. Lett. **121**, 176601 (2018).

[27] J. Martin and R. Gruehn, Solid State Ionics **43**, 19 (1990).

[28] C. Zhang, C. Guo, H. Lu, X. Zhang, Z. Yuan, Z. Lin, J. Wang, and S. Jia, Phys. Rev. B **92**, 041203(R) (2015).

[29] L. D. Landau, E. M. Lifshitz, and L. P. Pitaevskii, *Electrodynamics of Continuous Media*, 2nd edition, (Butterworth-Heinemann, Oxford, 1984).

[30] M. Dressel and G. Grüner, *Electrodynamics of Solids* (Cambridge University Press, Cambridge, 2002).

[31] D. B. Tanner, Phys. Rev. B **91**, 035123 (2015).

[32] M. B. Schilling, A. Löhle, D. Neubauer, C. Shekhar, C. Felser, M. Dressel, and A. V. Pronin, Phys. Rev. B **95**, 155201 (2017).

[33] M. B. Schilling, L. M. Schoop, B. V. Lotsch, M. Dressel, and A. V. Pronin, Phys. Rev. Lett. **119**, 187401 (2017).

[34] A. B. Kuzmenko, Rev. Sci. Instrum. **76**, 083108 (2005).

[35] G. Chanda, R. P. S. M. Lobo, E. Schachinger, J. Wosnitza, M. Naito, and A. V. Pronin, Phys. Rev. B **90**, 024503 (2014).

[36] J. Xu, M. Greenblatt, T. Emge, P. Hohn, T. Hughbanks, and Y. Tian, Inorg. Chem. **35**, 845 (1996).

[37] O. K. Andersen, Phys. Rev. B **12**, 3060 (1975).

[38] V. Antonov, B. Harmon, and A. Yaresko, *Electronic Structure and Magneto-Optical Properties of Solids* (Kluwer Academic Publishers, Dordrecht, Boston, London, 2004).

[39] J. P. Perdew and Y. Wang, Phys. Rev. B **45**, 13244 (1992).

[40] P. E. Blöchl, O. Jepsen, and O. K. Andersen, Phys. Rev. B **49**, 16223 (1994).

[41] D. Chaudhuri, B. Cheng, A. Yaresko, Q. D. Gibson, R. J. Cava, and N. P. Armitage, Phys. Rev. B **96**, 075151 (2017).

[42] B. Xu, Y. M. Dai, L. X. Zhao, K. Wang, R. Yang, W. Zhang, J. Y. Liu, H. Xiao, G. F. Chen, S. A. Trugman, J.-X. Zhu, A. J. Taylor, D. A. Yarotski, R. P. Prasankumar, and X. G. Qiu, Nat. Commun. **8**, 14933 (2017).

[43] D. Chang, Y. Liu, F. Rao, F. Wang, Q. Sunac, and Y. Jia, Phys. Chem. Chem. Phys. **18**14503, (2016).

[44] H. W. Liu, P. Richard, L. X. Zhao, G.-F. Chen, and H. Ding, J. Phys. Condens. Matter **28**, 295401 (2016).

[45] D. Wu, N. Barišic, P. Kallina, A. Faridian, B. Gorshunov, N. Drichko, L. J. Li, X. Lin, G. H. Cao, Z. A. Xu, N. L. Wang, and M. Dressel, Phys. Rev. B **81**, 100512(R) (2010).

[46] R. P. S. M. Lobo, G. Chanda, A. V. Pronin, J. Wosnitza, S. Kasahara, T. Shibauchi, and Y. Matsuda, Phys. Rev. B **91**, 174509 (2015).

[47] D. Neubauer, A. V. Pronin, S. Zapf, J. Merz, H. S. Jeevan, W.-H. Jiao, P. Gegenwart, G.-H. Cao, and M. Dressel, Phys. Status Solidi B **254**, 1600148 (2017).

[48] A. J. Frenzel, C. C. Homes, Q. D. Gibson, Y. M. Shao, K. W. Post, A. Charnukha, R. J. Cava, and D. N. Basov, Phys. Rev. B **95**, 245140 (2017).

[49] P. Y. Yu and M. Cardona, *Fundamentals of Semiconductors: Physics and Materials Properties* (Springer, Berlin, 2010).

[50] C. J. Tabert and J. P. Carbotte, Phys. Rev. B **93**, 085442 (2016).

[51] F. Arnold, C. Shekhar, S.-C. Wu, Y. Sun, R. D. dos Reis, N. Kumar, M. Naumann, M. O. Ajeesh, M. Schmidt, A. G. Grushin, J. H. Bardarson, M. Baenitz, D. Sokolov, H. Borrmann, M. Nicklas, C. Felser, E. Hassinger, and B. Yan, Nat. Commun. **7**, 11615 (2016).